Role of Cyclopentyl methyl ether co-solvent in Improving SEI layer stability in Hard Carbon Anode for Sodium-ion Batteries

Authors: Nagmani [a], Dhrubajyoti Das and Sreeraj Puravankara [a*]

Affiliations: [a] School of Energy Science & Engineering, Indian Institute of Technology Kharagpur, Kharagpur -721302, West Bengal, India

Corresponding author: Dr. Sreeraj Puravankara

School of Energy Science & Engineering, IIT Kharagpur,

Kharagpur -721302, West Bengal, India

Phone (Office) - +913222 260801

email: sreeraj@iitkgp.ac.in

ORCID ID

Nagmani: https://orcid.org/0000-0003-4618-4952

Dhrubajyoti Das: https://orcid.org/0000-0001-6435-3807

Sreeraj Puravankara: https://orcid.org/0000-0002-9238-0148

Abstract:

Upcycling plastic waste into value-added products helps to generate cost-effective and sustainable resources towards a circular materials economy and safer ecosystem. The conversion of polyethylene terephthalate (PET) municipal waste via the carbonization process into hard carbon (WPET-HC) delivers a high-performing, low-cost, sustainable anode material for sodium-ion batteries (SIBs). To further optimize the anode, electrolytes and interfacial chemistry are critical in improving cycling stability and rate capability. Herein, cyclopentyl methyl ether (CPME), a weakly solvating and a wide temperature solvent, is used as an alternative co-solvent to ethylene carbonate (EC) to deliver a high initial coulombic efficiency (ICE) up to 75%. The larger interlayer spacing, low surface area, and slit-shaped micro and mesoporous presence in the WPET-HC structure enhance the low potential plateau capacity to 68%, showing a more battery-type anode material from plastic trash. The WPET-HC delivered the excellent reversible capacity of 356 mAh g^{-1} at the current density of 30 mA g^{-1} with superior cycling of 91% after 100 cycles using CPME-PC-based electrolyte. The reduction of CPME co-solvent forms a more inorganic SEI than EC-generated SEI, providing a stable and thin SEI layer boosting the ICE and cycling stability of the anode. The low-temperature battery metric for CPME-PC-based electrolytes showed ~30% added capacity and improved ICE value compared to EC-PC-based electrolytes. The CPME-PC-based electrolyte maintained the higher capacity retention of 88% and 74% at 10℃ and 0℃, respectively, with a coulombic efficiency of 100%, revealing the excellent stability of the electrolyte with the HC anode. The work provides an eco-friendly approach to developing hard carbons from plastic trash and reports for the first time the use of greener, low-solvating CPME in improving the reversible capacity and ICE for low-temperature applications of SIBs.

Keywords: sodium-ion batteries; upscaled PET plastic waste; hard carbon anode; plateau capacity; cyclopentyl methyl ether; SEI design.

Introduction:

Sodium-ion batteries (SIBs) have gained much attention as alternative candidates for large-scale stationary energy storage due to the abundance of sodium resources. The design of low-cost, high-performance electrode materials is a key to endorsing their future commercialization. Fortunately, several excellent performing cathode materials have been reported, such as layered oxides,[1,2] phosphates,[3] sulfates[4], and Prussian blue analogs.[5] However, the demand and optimization of anode materials remain a significant challenge for commercialization.[6] Alloy-based anodes suffer from massive volume expansion during metal ion insertion, leading to fast capacity decay. In contrast, organic compounds have poor electronic conductivity resulting in low initial Coulombic efficiency and poor capacity retention.[7] Graphite is the commercial choice for the anode in LIBs. However, it is unsuitable for commercial sodium storage due to the thermodynamic instability of GICs.[8,9] The most investigated anode for SIBs is hard carbon (HC), also known as non-graphitizable carbon,[10] delivers a specific capacity >300 mAh g^{-1} with superior rate capability and cycling stability.[11,12] The diverse precursors used to synthesize low-cost HC anode are sugar, biomass, and organic polymers.[12,13]

Alternatively, the state-of-the-art approaches for recycling plastic waste into hard carbon as value-added materials help to generate new resources and reduce environmental pollution. The global consumption statistics show that the volume of plastic production exceeded 368 million metric tons with an annual CAGR of ≈ 5%, thus leading to massive plastic waste and generating enormous amounts of greenhouse gases (GHGs).[14] Carbonization, gasification, and catalytic pyrolysis hydrogenation are the economic techniques for using waste plastic for many applications, such as adsorbent for water purification, hydrogen storage, and energy storage devices.[15–19]

Besides the material designs, electrolyte compatibility was crucial in enhancing electrochemical performance. Conventional carbonate-based esters such as ethylene carbonate (EC), propylene carbonate (PC), diethyl carbonate (DEC), and dimethyl carbonate (DMC) are widely used organic solvents for SIBs.[20] EC is a go-to solvent/co-solvent due to the high polarity and dielectric constant (~90 at 40°C), ensuring complete salt dissociation. But the unstable (dissolving), richer organic SEI layer results in poor initial Coulombic efficiency (ICE) and capacity decay during cycling.[20,21] The low-temperature performance of EC is worse (liquid temperature range is poor) and is used in combination with other co-solvents for low-temperature battery applications. Recently, CPME-based solvents were reported for low-temperature Li-ion and ambient Li-metal batteries. The eco-friendly green CPME is a weakly solvating solvent with a wide liquid-phase temperature range of -140 °C to 106 °C.[21,22] No such reports are available for Na-ion batteries.

As an alternative to EC, the low-solvating cyclopentyl methyl ether (CPME) in combination with PC was studied to improve the anode characteristics of WPET-HC for SIBs. Herein, the WPET-HC with CPME-PC-based electrolyte shows a high reversible capacity of 356 mAh g^{-1} with high ICE of 74.5%. The changes in reversible capacity and ICE while switching from EC to CPME were similar at ambient and higher temperatures (~ 40°C). However, performance improves by more than 30% at a lower temperature (~ 0°C) with excellent cycling stability. In addition, the larger interlayer spacing, low surface area, and slit-shaped micro and mesoporous presence in the HC structure enhance the low potential plateau capacity to 68%, providing a more battery-type anode material from plastic trash.

Experimental Section:

Synthesis of Hard Carbon: PET-based plastic waste (packaged drinking water bottles supplied by railways) was used without further purification to synthesize hard carbon by direct pyrolysis. The carbonization was done using a quartz tube furnace at 1000°C for two hours in

the N_2 atmosphere at a heating rate of 4℃ min^{-1}. The obtained HCs product was ground manually and denoted as WPET-HC.

Material Characterization: The morphology and microstructure of the HCs were investigated by field-emission gun-scanning electron microscopy (FEG-SEM, ZEISS Sigma 300) and analytical transmission electron microscopy (Technai G2-20 TEM). X-ray diffraction (XRD) was conducted on Bruker-D2 Phaser instrument with Cu Kα (λ = 1.5418 Å) radiation to calculate the graphene bilayer spacing and crystallite size using the Bragg equation and Scherrer equation. Raman spectra were carried out between 1000 cm^{-1} to 2000 cm^{-1} on a Horiba T6400 with a 514.5 nm Ar-Krypton mixed ion gas laser. Further, Fourier transforms infrared spectrometer (FT-IR) was carried out on Thermo Fisher Scientific Instruments to investigate the available functional groups. The Brunauer-Emmett-Teller (BET) surface area and pore-size distribution of the WPET-HC were analyzed using an N_2 adsorption isotherm at 77 K with an outgassing temperature of 250 ℃ (Autosorb IQ instrument). X-ray photoelectron spectroscopy (XPS) measurement was performed on PHI 5000 VERSA PROBE III (ULVAC PHI(Physical Electronics), USA) using a monochromatic Al K_α X-Ray Source. The SAXS experiment was performed using a XENOCS SAS instrument using synchrotron radiation as the X-ray source (30 W Cu tube with 50KV, 0.6 mA).

Electrochemical Characterization: The PET-based hard carbon anode was prepared by a homogeneous mixture of active material, Super-P black carbon, and polyvinylidene difluoride (PVDF) in the ratio of 80:10:10 with N-methyl-2-pyrrolidone solvent using THINKY mixer instrument. The obtained slurry was uniformly coated onto a copper (Cu) foil with an anode mass loading of ~ 2 mg cm^{-2} and dried at 80℃ for 12 h in a vacuum oven. Further, the CR-2032 coin cell was fabricated inside the Ar-filled glovebox (M-Braun, H_2O < 0.5 ppm; O_2 < 0.5 ppm), using sodium metal as the counter electrode and Whatman glass fiber membrane (GF/C) as the separator between two electrodes. The carbonate ester-based electrolyte used

was 1M $NaClO_4$ in a binary mixture of ethylene carbonate (EC) and propylene carbonate (PC) (1:1, v/v) for Na cells. In addition, the EC was replaced by cyclopentyl methyl ether (CPME), and a mixture ether/ester solvent as CPME: PC (1:1, v/v) with 1M $NaClO_4$ salt was used as electrolyte. The galvanostatic discharge-charge (GCD) cycling at different current densities and cyclic voltammetry (CV) measurement at different scan rates were tested on a Bio-Logic instrument in the potential range of 1.5 to 0.005V. The GITT technique was performed at the second cycle by applying a pulse current of 30 mA g^{-1} for 30 min with an intermittent equilibrium of 1 hour. The sodium-ion diffusion coefficients (D_{Na^+}) were estimated by solving Fick's second law[23,24] using the simplified equation (1).

$$D = \frac{4}{\pi\tau}\left(\frac{m_B V_B}{M_B S}\right)^2 \left(\frac{\Delta E_S}{\Delta E_\tau}\right)^2 \qquad (1)$$

where M_B and m_B are the molar mass of hard carbon and the mass of the electrode material, respectively. V_B is the molar volume; S is the active surface area of the electrode material, τ is the pulse duration; ΔE_S and $\Delta E\tau$ can be obtained from the GITT curve. Electrochemical impedance spectroscopy (EIS) measurements were performed in a frequency range from 10 mHz to 10 kHz. GCD profiles and CV from 0°C to 40°C were carried out for temperature-dependent studies for electrolyte systems at different current densities.

Results and Discussion

Material Characterization: Hard carbon was synthesized by direct pyrolysis of waste PET under the N_2 atmosphere. The proposed synthesis pathway of PET-based carbonized hard carbon is illustrated in Figure S1. The cross-linked PET undergoes chain scission, decarbonylation, and condensation/dehydrogenation reactions during carbonization.[16,25] The chain scission of the C-O bond on the ester group through decarbonylation to release CO/CO_2 is associated with the materialization of cross-linking to form high carbon content solid hydro char. Figure S2 shows the FT-IR spectra, and the presence of the carbonyl ester group (C=O)

at wave number ~1740 cm^{-1} (position: 4) confirms the C-O bond scission into ester groups and further decarbonylation to hydro char from PET.[26,27]

The peak at ~2922 cm^{-1} corresponds to –CH and the peaks between 1550 to 1650 cm^{-1} belonged to the C=C of the benzene ring to support the presence of benzenoid compounds.[28] The peak near 1200 cm^{-1} is ascribed to the terephthalate group ($OOCC_6H_4$-COO) due to the cross-linking of PET during carbonization.[29,30] Table S1 details the IR peaks observed with the functional group moieties on hard carbon obtained from WPET carbonized at 1000°C. The observations lead to the proposed scheme (S1) of PET conversion to HCs containing O-based functional groups at the surface.

FEG-SEM and analytical TEM examined the morphology and microstructure of the HC. The WPET-HC has bulky micro-stone-chips-like morphology (Figure 1a) with a particle size >30 µm. Interestingly, the morphology of raw WPET (Figure S3) has a homogeneous and smooth fractured surface that follows a decarbonylation reaction during the carbonization process and forms stone-chip morphology-based hydro char. The TEM image (Figure S4a) shows the highly dense carbon with a particle size in the micro-scale range. The turbostratic curves with randomly oriented graphene platelets were observed in HR-TEM images (Figure S4b,c). In addition, the SAED pattern of WPET-HC shows the dispersive diffraction ring, which confirms the amorphous nature (Figure S4d). The XRD pattern further confirmed the disordered structure shows two broad peaks near 23º and 43º corresponding to (002) and (100) planes, respectively (Figure 1b). The (002) peak of HCs is broader, but the peak position of WPET-HC was at a lower angle, signifying larger interlayer spacing of 0.379 nm, and are larger than that of graphite (~0.340 nm). The interlayer spacing is found to be pretty similar to that obtained from HR-TEM micrographs. Figure 1c shows the Raman spectra of the WPET-HC, revealing the graphitic characterization by estimating the two broad peaks at ~ 1350 cm^{-1} and 1590 cm^{-1}, corresponding to D-band and G-band, respectively.[31] The relative integrated

intensity ratio of the D (defects) and G (graphitic) bands is directly proportional to the defect concentration in the HCs. The I_D/I_G ratio of WPET-HC at 1000℃ is low compared to the WPET-HC samples carbonized at low temperature (800℃), as shown in Table S2, confirming more ordering of graphitic domains and less defect concentration at higher carbonization temperature.

XPS was used to gain insight into the functional substituents in the hard carbon synthesized at different temperatures. The turbostratic curve of HC has many defects and includes oxygen elements due to impurities in the precursor. The C1s deconvoluted XPS spectra (Figure 1d and S5) revealed the carbon and oxygen content in the WPET-HC. The oxygen content (at.%) decreases from 37.52% to 16.86% when the carbonization temperature increases from 800℃ to 1000℃. The deconvolution of the C1s peaks of XPS spectra show four separated peaks centered at 284.2, 285.1, 286, and 286.78 eV corresponding to sp^2 hybridized carbon, sp^3 hybridized carbon (defected/amorphous carbon), carbon-oxygen linkage (C-O), and C=O, respectively.[32–34] The reduction of sp^3 hybrid carbon (C-C) and carbon-oxygen (C-O, C=O) linkages[33] with the temperature rise suggests more graphitization and less defect for WPET-HC, as supported by XRD and RAMAN analysis.

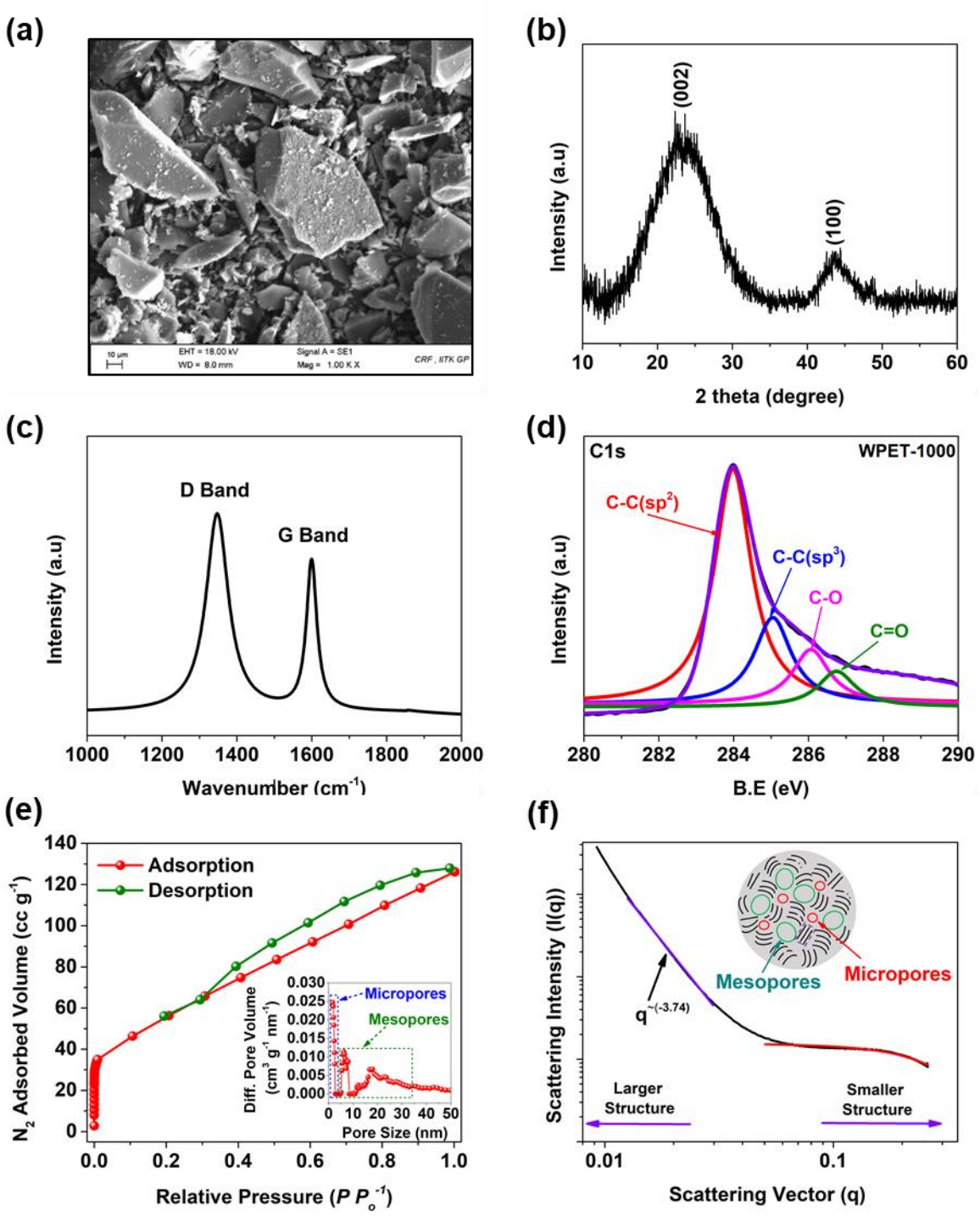

Figure 1: Morphology and structural features of WPET-HC: (a) FEG-SEM image (b) XRD pattern, (c) Raman spectra, (d) Deconvolution of the C1s peaks of XPS spectra (e) N_2 adsorption isotherm (inset: Pore size distribution:), and (f) SAXS pattern.

The turbostratic (non-periodic stacking) curved hard carbon generates many differently sized open and closed pores. Figure 1e shows the nitrogen-adsorbed isotherm profile. WPET-HC

shows Type-II isotherm at high pressure with type-H4 hysteresis due to capillary condensation, commonly associated with partially closed slit-shaped pores[35] lying in the microporous/mesoporous region. The low BET surface area (SA) of WPET-HC is 205 $m^2 g^{-1}$ (pore volume of 0.186 $cm^3 g^{-1}$) is beneficial for less decomposition of electrolytes during initial cycles and stable solid electrolyte interface (SEI) layer formation. The pore-size distribution revealed the presence of both micro and mesopores in the structure, as shown in Figure 1e (inset). Besides, the micropore volume of WPET-HC is 3×10^{-2} $cm^3 g^{-1}$, which concludes that 84% of mesoporosity results in a hierarchical and continuous network of micro- and mesopores, improving the ion diffusion channels within the HC structure. The presence of more mesopores can contribute to additional charge storage from the pore-filling at the confined slit-shaped nanopores. In addition, SAXS was used to investigate the pore structure further, as the gas adsorption studies were sensitive to the surface open pores. Figure 1f shows the typical SAXS profile with the fitted curve at low and high scattering vector regions. At low q region (0.01-0.05 $Å^{-1}$), the intensity drops as $q^{-\alpha}$, where α is 3.74, close to 4, typical for sharp interfaces of larger objects (macro and mesopores) with almost spherical in morphology. Further, at the intermediate q region (0.07-0.2 $Å^{-1}$), the intensity evolution shows a plateau followed by a kink, indicating the presence of micropores.[36] Later, the Guinier analysis and Porod's law method were used to quantify the porous characterization of the WPET-HC (*see supporting information for more detail*).[37,38] Using the Porod method (Figure S6), the total surface area (SA_{SAXS}) was estimated as 575 $m^2 g^{-1}$, signifying more closed SA of 370 $m^2 g^{-1}$ than the open SA. Furthermore, the average pore diameter was estimated to be ~1.25 nm. In contrast, the gas isotherm method measured the pore diameter to be ~3.78 nm, suggesting the dominance of larger open and smaller-sized closed pores. Figure S7 shows the structural schematic of a WPET-derived hard carbon particle comprised of randomly aligned stacked graphene sheets with slit-shaped open pores.

Electrochemical Characterization: The galvanostatic discharge/ charge profile of WPET-HC anode vs. Na/Na^+ half cells using $NaClO_4$ salt in EC-PC and CPME-PC binary solvent are shown in Figure 2a-b. Using an EC-PC-based electrolyte, WPET-HC delivered the reversible capacity to 337 mAh g^{-1} with an initial coulombic efficiency (ICE) of 66%. In contrast, using a CPME-PC-based electrolyte as an EC-free solvent, WPET-HC significantly enhanced the ICE value to 74.5% with a reversible capacity of 356 mAh g^{-1}. The CPME (ether) solvent mixture with PC induces lower desolvation energy, which is attributed to faster charge-transfer kinetic and is partially responsible for excellent performance.[21,22] The charge/discharge profile shows that the WPET-HC exhibits a greater plateau region, significantly below 0.1 V, indicating intercalation followed by closed-pore filling. To quantify the maximum plateau-based capacity for WPET-based HC, typical derivative capacity (*dQ/dV*) curves were analyzed, as shown in Figure 2c. The WPET-HC using EC-PC/ CPME-PC-based electrolyte, exhibits strong sodiation and desodiation peaks at 0.0511/ 0.0548 and 0.0913/ 0.0845 V, respectively. As reported, these peaks correspond to the defect-assisted insertion/pore filling in the hard carbon anodes.[11,39] After that, the first reversible capacity was spitted into the sloping and plateau capacity based on the sodiation peaks at a lower potential, as shown in Figure 2c (inset). The surface adsorption-based sloping capacity (SRC) is marginally better for CPME-PC, and PRC contributions were similar for both systems. The better SRC can also be due to the faster charge transfer kinetic using the ether/ester combination.[22,40,41] The capacitive and diffusion contribution was quantified using the CV curve, as shown in Figure S8. The capacitive contribution for CPME-PC-based electrolytes is marginally better than EC-PC-based electrolytes and increases with the scan rate to support the better SRC value. However, the WPET-HC, with its more hierarchical porosity distribution, favors more nanopore-filling and promotes a significantly higher plateau capacity of 68%, suggesting typical battery type, lower insertion potential, and sustainable anode material from PET plastic waste for SIBs. Table S3

summarizes the reported plastic-waste and biomass precursor-based HC and their comparative electrochemical properties for SIBs. The HC anode WPET-HC shows the best reversible capacity with maximum plateau capacity contribution for sodium-ion batteries signifying a promising battery-type anode for SIBs.

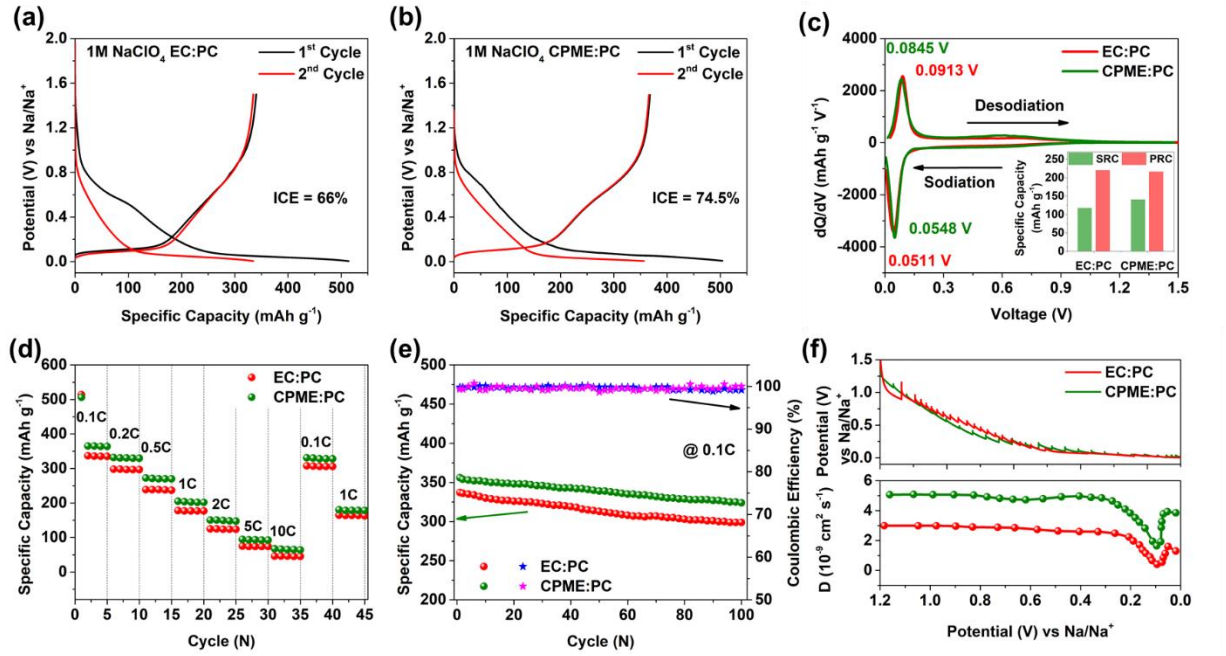

Figure 2: Discharge-charge profile at 0.1C rate of WPET-HC in (a) EC-PC, (b) CPME-PC system. (c) Differential capacity-voltage curve (inset: plateau and sloping capacity distribution. (d) Rate performance, and (e) Long cycle stability at 0.1C rate. (f) GITT curve and diffusion coefficient as a function of potential.

The superior rate performance of WPET-HC electrodes at various current rates is shown in Figure 2d. The specific discharge capacities of 337/356, 298/326, 239/272, 180/202, 125/150, 75/94, and 46/67 mAh g^{-1} are recorded at 0.1C, 0.2C, 0.5C, 1C, 2C, 5C, and 10C rates, respectively for EC-PC and CPME-PC-based electrolyte. The reversible capacity retention of 91.5% and 93.2% was achieved after 35 cycles of the rate test for EC-PC and CPME-PC, respectively, signifying excellent electrode stability and supporting the long cycle data at a 0.1C rate. The WPET-HC anodes demonstrated highly reversible and repeatable voltage

profiles. Figure 2e confirms that the WPET-HC electrodes exhibit excellent reversible capacity retention of 88% (EC:PC) and 91% (CPME:PC) between the 2nd and 100th cycles. Also, the stability of SEI is reflected by achieving almost 100% Coulombic efficiency after the initial cycle.

GITT was used to calculate the diffusion coefficient and to explore the ion kinetics and storage mechanism in the WPET-HC anode. As shown in Figure 2f, during the sodiation process, the D_{Na}^{+} decreases slowly (*1.2-0.2 V:*), followed by a sharp decline to ~0.08 V (D_{Na}^{+}*: 4.5 × 10^{-10} cm^2 s^{-1} for EC-PC and 1.64 × 10^{-9} cm^2 s^{-1} for CPME-PC*). Further, the D_{Na}^{+} recovers increases sharply and then drops till the cut-off potential (0.005 V). In the potential range of 1.2-0.2 V, the slow decline of D_{Na}^{+} is associated with the sizeable repulsive force generated among Na-ion adsorbed in the active sites,[42,43] then sharp decline (0.2-0.08 V) is due to unstable Na-rich graphitic intercalation compound.[8,44] The lowest D_{Na}^{+}, mainly concentrated in the plateau region, indicates a sluggish electrochemical reaction. Here, the D_{Na}^{+} of CPME-PC is more than an order of magnitude higher than EC-PC, suggesting better reaction kinetic due to the low desolvation energy of CPME.[45–48]

To gain insight into the evolution of SEI films and the kinetics difference of Na^+ storage for different electrolytes, ex-situ XPS, FTIR, and XRD were employed. Figure 3a-c shows the systematic XPS analysis to investigate the surface chemistry of the cycled WPET-HC electrode at a current density of 30 mAh g^{-1} for EC-PC and CPME-PC-based electrolyte and their effects on the electrochemical performance. The C1s spectrum in both electrolyte display five peaks located at 283.6 eV (Na_x-HC), 285.28 eV (C-C/C-H), 287.1 eV (C-O), 288.6 eV (C=O), and 291.3 eV (CO_3).[49,50] Notably, the SEI layer's organic content (–C=O, -C-O-) is lower for the CPME-PC-based electrolyte. The CO_3 species arise from the solvent-derived SEI components, which are significantly reduced for CPME-PC, and a salt-derived inorganic SEI is observed, as seen in the Cl-2p spectrum (Figure 3c).[21] The higher Nax-HC and C-C peak intensity appears

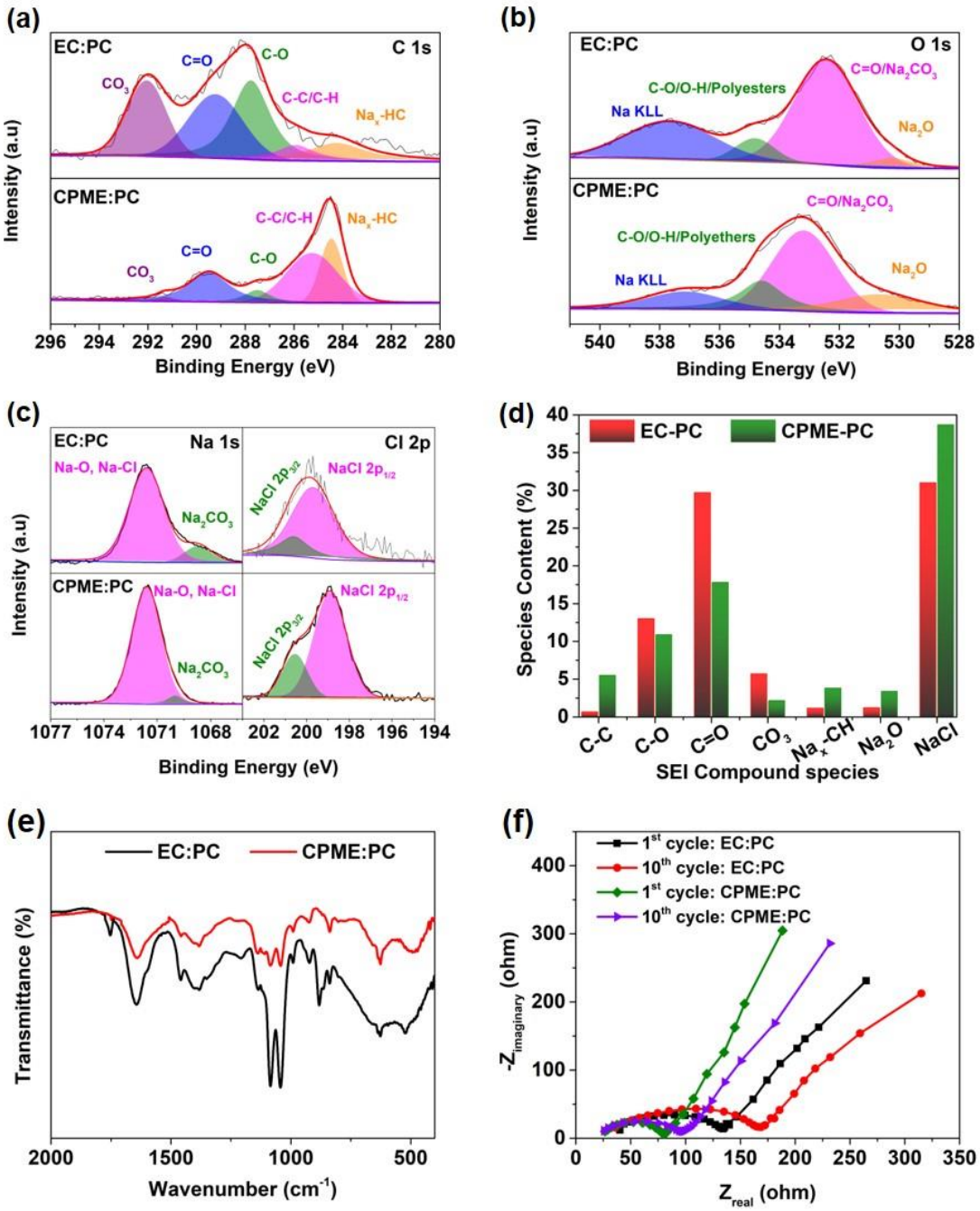

Figure 3: XPS spectra for a cycled HC in EC-PC and CPME-PC-based electrolyte: (a) C 1s, (b) O 1s, and (c) Na 1s & Cl 2p (d) SEI components (%) from XPS (e) FTIR spectrum of cycled HC anode (e) Nyquist plots of HC after the 1st and 10th cycle.

in the C1s spectrum for CPME-PC-based electrolytes, indicating a thinner SEI film formation.[49,50] The peaks at 198.9 eV and 200.5 eV in Cl 2p spectrum arise from the Na-Cl species in the SEI, whereas the peaks at higher binding energy indicate organic chlorine

covalently bonded to sp^2-C or Cl-C=O bonds.[51,52] In summary, the Na-containing inorganic components, especially Na_2O and NaCl, are higher, but O-containing substituents are lower for CPME-EC-based electrolytes suggesting a more compact and stable SEI layer, which can restrict the continuous decomposition of electrolytes. The resulting thin SEI will effectively decrease the Na^+ diffusion length and charge-transfer resistance and boost the electrochemical performance. The variation in SEI composition (%) for both the electrolyte system is shown in Figure 3d. To further explore the more organic species-based SEI components in EC-PC-based electrolytes, ex-situ FTIR was employed, as shown in Figure 3e. The peak characteristics of organic-based species of EC-PC-based electrolytes are stronger than CPME-PC-based electrolytes, which supports the XPS analysis of a thinner, more inorganic, and more stable SEI film formation for the CPME-PC system.

The growth of SEI during cycling was investigated using EIS measurements. The EIS profiles at 0.1C display the one semicircle occurring at high/medium frequencies, representing the resistance due to SEI film (R_{SEI}) and charge transfer (R_{CT}) with Warburg impedance (W) originating from Na^+ semi-infinite diffusion.[53] As shown in Figure 3f, the electrolyte solution resistance (R_S) is 21 Ω for CPME-PC, but ~ 34 Ω for EC-PC, indicating rapid migration of Na^+ in ether-ester combination. Besides, for the EC-PC electrolyte system, the resistance (R_{SEI} + R_{CT}) is almost 40% higher than the CPME-PC electrolyte, suggesting a slower transfer kinetics from the higher desolvation energy of EC.[54] In CPME-PC-based electrolyte, the resistance (RSEI + RCT) increase after ten cycles is 26% lower than that of EC-PC-based electrolyte, indicating stable, inorganic SEI film, which provides effective passivation for the HC-anode by reducing the anode polarization and improving cyclability.

To gain insight into the amount of Na^+ intercalation into HC with two different electrolytes, ex-situ XRD was performed on the discharged electrode. The broad (002) peak shifts to a lower

angle in the case of CPME-PC-based electrolyte, possibly due to the lower desolvation energy of the CPME.[21,22]

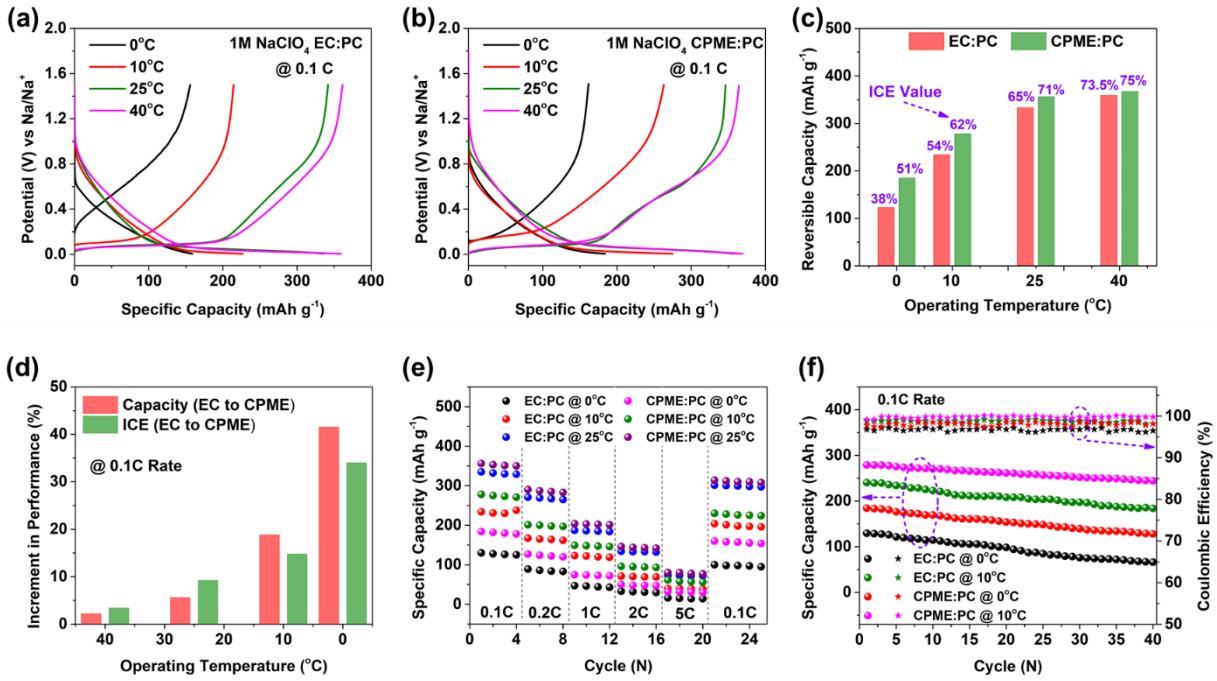

Figure 4: (a) Charge-discharge profiles at 0.1C rate of WPET-based HC at different cell operating temperatures in (a) EC-PC, (b) CPME-PC system. (c) Reversible capacity and ICE (%) as a function of cell operating temperature. (d) Performance improvement from EC:PC to CPME:PC electrolyte system at 0.1C rate. (e) C-rate performance, and (f) Cycle stability for both electrolyte systems at different cell operating temperatures.

Effect of Cell Operating Temperature: The evolution of CPME co-solvent with temperature, the EC-free solvent was measured in a thermal chamber from 0°C to 40°C. Figure 4a,b shows the GCD profiles at 0.1C rate. A comparable reversible capacity of 333 mAh g^{-1} (EC-PC) and 353 mAh g^{-1} (CPME-PC) was achieved at 25°C. The reversible capacity, PRC, and ICE value followed a decreasing trend as the cell operating temperature dropped 0°C, as shown in Figure 4c. In contrast, the reversible capacity, PRC, and ICE value of WPET-HC using CPME-PC outperform the EC-PC at cell operating temperatures of 10°C and 0°C due to the wider liquid range and better transport properties of CPME solvent. Excellent low-temperature performance

of 278/234 mAh g^{-1} and 185/130 mAh g^{-1} for CPME-PC/EC-PC-based electrolyte at cell operating temperatures of 10℃ and 0℃, respectively.

Further, this improvement in the electrochemistry performance at 0.1C rate was analyzed at different operating temperatures, as displayed in Figure 4d. The changes in capacity and ICE, while switching from EC to CPME, are similar at 40℃, although the increment in performance is more than 30% at lower temperatures. CPME co-solvent achieves more favorable interfacial properties to show a high ICE value of up to 80% from its low solvating nature and the chemical stability of the cyclic alkyl group at lower temperatures.[22] Figure 4e shows the rate performance of these electrolytes at different current rates. The capacities for CPME-PC-based electrolytes are higher till the 2C rate due to lower charge transfer resistance, faster desolvation process, and stable, robust SEI film formation.

Interestingly, at the higher 5C rate, the difference in capacities for both electrolyte systems is negligible, as the capacitive storage mechanism becomes more dominant with increasing C-rate. After 40 cycles, the EC-PC-based electrolyte showed a capacity retention of 77% (10℃), and 51% (0℃), whereas the CPME-PC-based electrolyte could maintain a high capacity retention of 88% and 74% at 10℃ and 0℃, respectively, with 100% Coulombic efficiency.

Conclusion

In summary, we report the upcycling of PET-based plastic waste for the high-performance anode in SIBs and explore the application of CPME solvent as an alternative to EC. The WPET-HC delivered the excellent reversible capacity of 356 mAh g^{-1} at the current density of 30 mA g^{-1} with superior cycling of 91% after 100 cycles using CPME-PC-based electrolyte. The unique features of HC, such as larger interlayer spacing, low surface area, and slit-shaped micro and mesopores in the structure, enhance the low potential plateau capacity to 68%, indicating battery-type anode material from plastic trash. Further, we compared the performance

difference between the EC-PC (ester-ester) and CPME-PC (ether-ester)-based electrolyte through XPS, FTIR, XRD, and EIS measurements during and after CD cycles. The Na-containing inorganic components, especially Na_2O and NaCl species, were higher, and O-containing substituents were lower for CPME-EC-based electrolytes. The SEI film was more inorganic and stable, restricting the continuous dissolution of the SEI layer as found in organic-rich SEI layers, thereby improving the ICE and cycling stability of the anode. A thinner SEI effectively decreases the Na^+ diffusion length and charge-transfer resistance and further boosts the electrochemical kinetics. In addition, excellent low-temperature performance was observed for CPME-PC-based electrolytes with ~30% added capacity and ICE value compared to EC-PC-based electrolytes. The CPME-PC-based electrolyte maintained the higher capacity retention of 88% and 74% at 10℃ and 0℃, respectively, with the coulombic efficiency of 100%, due to the robust SEI layer on the HC anode. This study paves the way for a less energy-intensive approach for utilizing the waste PET conversion to HCs for sustainable anode material for sodium-ion batteries with distinct storage mechanisms. It offers a practical approach to designing co-solvents, especially for low-temperature applications for enhanced reversible capacity and high ICE for HC anodes in Na-ion batteries.

Acknowledgments

This work was supported by funding from the Tata Chemicals Society for Rural Development (TCSRD) (Grant No: PONIB001). Nagmani acknowledges IIT Kharagpur for a Ph.D. fellowship and provides the central research facilities for specific measurements. The authors acknowledge using battery testing facilities at Central Railway Research Institute and the Department of Electrical Engineering, IIT Kharagpur.

CRediT authorship contribution statement

Nagmani: Methodology, Investigation, Visualization, Formal analysis, Software, TOC, and Writing - original draft, review & editing.

Dhrubajyoti Das: Formal analysis, Software, TOC, and Writing - review & editing.

Sreeraj Puravankara: Conceptualization, Supervision, Visualization, Resources, Writing - review & editing, Funding Acquisition, and Project Administration.

Conflict of Interest

The authors declare no conflicts of interest in the reported work.

Data Availablity Statement

Data will be made available on request.

References

(1) Wang, P. F.; You, Y.; Yin, Y. X.; Guo, Y. G. Layered Oxide Cathodes for Sodium-Ion Batteries: Phase Transition, Air Stability, and Performance. *Adv. Energy Mater.* **2018**, *8* (8), 1–23. https://doi.org/10.1002/aenm.201701912.

(2) Guo, S.; Li, Q.; Liu, P.; Chen, M.; Zhou, H. Environmentally Stable Interface of Layered Oxide Cathodes for Sodium-Ion Batteries. *Nat. Commun.* **2017**, *8* (1), 1–9. https://doi.org/10.1038/s41467-017-00157-8.

(3) Kanwade, A.; Gupta, S.; Kankane, A.; Srivastava, A.; Yadav, S. C.; Shirage, P. M. Phosphate-Based Cathode Materials to Boost the Electrochemical Performance of Sodium-Ion Batteries. *Sustain. Energy Fuels* **2022**, *6* (13), 3114–3147. https://doi.org/10.1039/d2se00475e.

(4) L. Lander, J.-M. Tarascon, A. Y. Sulfate-based Cathode Materials for Li- and Na-ion Batteries.Pdf. **2018**, *18* (10), 1394-1408. https://doi.org/10.1002/tcr.201800071

(5) Tyagi, A.; Nagmani; Puravankara, S. Opportunities in Na/K [Hexacyanoferrate] Frameworks for Sustainable Non-Aqueous Na + /K + Batteries . *Sustain. Energy Fuels* **2022**, *6* (3), 550–595. https://doi.org/10.1039/d1se01653a.

(6) Nagmani, Pahari, D.; Verma, P.; Puravankara, S. Are Na-Ion Batteries Nearing the Energy Storage Tipping Point ? – Current Status of Non-Aqueous , Aqueous , and Solid-Sate Na-Ion Battery Technologies for Sustainable Energy Storage. *J. Energy Storage* **2022**, *56* (PA), 105961. https://doi.org/10.1016/j.est.2022.105961.

(7) Lao, M.; Zhang, Y.; Luo, W.; Yan, Q.; Sun, W.; Dou, S. X. Alloy-Based Anode Materials toward Advanced Sodium-Ion Batteries. *Adv. Mater.* **2017**, 29, 1700622. https://doi.org/10.1002/adma.201700622.

(8) Moriwake, H.; Kuwabara, A.; Fisher, C. A. J.; Ikuhara, Y. Why Is Sodium-Intercalated Graphite Unstable? *RSC Adv.* **2017**, *7* (58), 36550–36554. https://doi.org/10.1039/c7ra06777a.

(9) Nobuhara, K.; Nakayama, H.; Nose, M.; Nakanishi, S.; Iba, H. First-Principles Study of Alkali Metal-Graphite Intercalation Compounds. *Journal of Power Sources*. **2013**, pp 585–587. https://doi.org/10.1016/j.jpowsour.2013.06.057.

(10) Nagmani; Kumar, A.; Puravankara, S. Optimizing Ultramicroporous Hard Carbon

Spheres in Carbonate Ester-based Electrolytes for Enhanced Sodium Storage in Half-/Full-cell Sodium-ion Batteries. *Batter. Energy* **2022**, *1* (3), 0220007. https://doi.org/10.1002/bte2.20220007.

(11) Nagmani; Puravankara, S. Insights into the Plateau Capacity Dependence on the Rate Performance and Cycling Stability of a Superior Hard Carbon Microsphere Anode for Sodium-Ion Batteries. *ACS Appl. Energy Mater.* **2020**, *3 (*10), 10045–10052. https://doi.org/10.1021/acsaem.0c01750.

(12) Nagmani; Tyagi, A.; Puravankara, S. Insights into the Diverse Precursor-Based Micro-Spherical Hard Carbons as Anode Materials for Sodium–Ion and Potassium–Ion Batteries. *Mater. Adv.* **2022**, *3* (2), 810–836. https://doi.org/10.1039/d1ma00731a.

(13) Thompson, M.; Xia, Q.; Hu, Z.; Zhao, X. S. A Review on Biomass-Derived Hard Carbon Materials for Sodium-Ion Batteries. *Mater. Adv.* **2021**, *2* (18), 5881–5905. https://doi.org/10.1039/d1ma00315a.

(14) Halden, R. U.; Rolsky, C.; Khan, F. R. Time: A Key Driver of Uncertainty When Assessing the Risk of Environmental Plastics to Human Health. *Environ. Sci. Technol.* **2021**, *55* (19), 12766–12769. https://doi.org/10.1021/acs.est.1c02580.

(15) Choi, J.; Yang, I.; Kim, S. S.; Cho, S. Y.; Lee, S. Upcycling Plastic Waste into High Value-Added Carbonaceous Materials. *Macromol. Rapid Commun.*, **2022**, *43*: 2100467. https://doi.org/10.1002/marc.202100467.

(16) Chia, J. W. F.; Sawai, O.; Nunoura, T. Reaction Pathway of Poly(Ethylene) Terephthalate Carbonization: Decomposition Behavior Based on Carbonized Product. *Waste Management*. **2020**, pp 62–69. https://doi.org/10.1016/j.wasman.2020.04.035.

(17) U.S. Deparment of Energy Office of Energy Efficiency & Renewable energy. Waste-to-Energy from Municipal Solid Wastes Report. **2019**.

(18) Kumar, U.; Goonetilleke, D.; Gaikwad, V.; Pramudita, J. C.; Joshi, R. K.; Sharma, N.; Sahajwalla, V. Activated Carbon from E-Waste Plastics as a Promising Anode for Sodium-Ion Batteries. *ACS Sustain. Chem. Eng.* **2019**, *7* (12), 10310–10322. https://doi.org/10.1021/acssuschemeng.9b00135.

(19) Chen, D.; Luo, K.; Yang, Z.; Zhong, Y.; Wu, Z.; Song, Y.; Chen, G.; Wang, G.; Zhong, B.; Guo, X. Direct Conversion of Ester Bond-Rich Waste Plastics into Hard

Carbon for High-Performance Sodium Storage. *Carbon*. **2021**, pp 253–261. https://doi.org/10.1016/j.carbon.2020.11.004.

(20) Ponrouch, A.; Marchante, E.; Courty, M.; Tarascon, J. M.; Palacín, M. R. In Search of an Optimized Electrolyte for Na-Ion Batteries. *Energy Environ. Sci.* **2012**, *5* (9), 8572–8583. https://doi.org/10.1039/c2ee22258b.

(21) Ramasamy, H. V.; Kim, S.; Adams, E. J.; Rao, H.; Pol, V. G. A Novel Cyclopentyl Methyl Ether Electrolyte Solvent with a Unique Solvation Structure for Subzero (−40 °C) Lithium-Ion Batteries. *Chem. Commun.* **2022**, *58* (33), 5124–5127. https://doi.org/10.1039/d2cc00188h.

(22) Zhang, H.; Zeng, Z.; Ma, F.; Wu, Q.; Wang, X.; Cheng, S.; Xie, J. Cyclopentylmethyl Ether , a Non-Fluorinated , Weakly Solvating and Wide Temperature Solvent for High-Performance Lithium Metal Battery Angewandte. **2023**, *202300771*. https://doi.org/10.1002/anie.202300771.

(23) Wang, K.; Jin, Y.; Sun, S.; Huang, Y.; Peng, J.; Luo, J.; Zhang, Q.; Qiu, Y.; Fang, C.; Han, J. Low-Cost and High-Performance Hard Carbon Anode Materials for Sodium-Ion Batteries. *ACS Omega* **2017**, *2* (4), 1687–1695. https://doi.org/10.1021/acsomega.7b00259.

(24) Jin, Y.; Sun, S.; Ou, M.; Liu, Y.; Fan, C.; Sun, X.; Peng, J.; Li, Y.; Qiu, Y.; Wei, P.; Deng, Z.; Xu, Y.; Han, J.; Huang, Y. High-Performance Hard Carbon Anode: Tunable Local Structures and Sodium Storage Mechanism. *ACS Appl. Energy Mater.* **2018**, *1* (5), 2295–2305. https://doi.org/10.1021/acsaem.8b00354.

(25) Huang, J. B.; Zeng, G. S.; Li, X. S.; Cheng, X. C.; Tong, H. Theoretical Studies on Bond Dissociation Enthalpies for Model Compounds of Typical Plastic Polymers. *IOP Conf. Ser. Earth Environ. Sci.* **2018**, *167* (1). https://doi.org/10.1088/1755-1315/167/1/012029.

(26) Ioakeimidis, C.; Fotopoulou, K. N.; Karapanagioti, H. K.; Geraga, M.; Zeri, C.; Papathanassiou, E.; Galgani, F.; Papatheodorou, G. The Degradation Potential of PET Bottles in the Marine Environment: An ATR-FTIR Based Approach. *Sci. Rep.* **2016**, *6* (October 2015), 1–8. https://doi.org/10.1038/srep23501.

(27) Dos Santos Pereira, A. P.; Da Silva, M. H. P.; Lima, É. P.; Dos Santos Paula, A.;

Tommasini, F. J. Processing and Characterization of PET Composites Reinforced with Geopolymer Concrete Waste. *Mater. Res.* **2017**, *20*, 411–420. https://doi.org/10.1590/1980-5373-MR-2017-0734.

(28) Zhao, Y.; Truhlar, D. G. Density Functionals with Broad Applicability in Chemistry. *Acc. Chem. Res.* **2008**, *41* (2), 157–167. https://doi.org/10.1021/ar700111a.

(29) Edge, M.; Wiles, R.; Allen, N. S.; McDonald, W. A.; Mortlock, S. V. Characterisation of the Species Responsible for Yellowing in Melt Degraded Aromatic Polyesters - I: Yellowing of Poly(Ethylene Terephthalate). *Polymer Degradation and Stability*. **1996**, pp 141–151. https://doi.org/10.1016/0141-3910(96)00081-X.

(30) Chen, Z.; Hay, J. N.; Jenkins, M. J. The Thermal Analysis of Poly(Ethylene Terephthalate) by FTIR Spectroscopy. *Thermochimica Acta*. **2013**, pp 123–130. https://doi.org/10.1016/j.tca.2012.11.002.

(31) Ferrari, A.; Robertson, J. Interpretation of Raman Spectra of Disordered and Amorphous Carbon. *Phys. Rev. B - Condens. Matter Mater. Phys.* **2000**, *61* (20), 14095–14107. https://doi.org/10.1103/PhysRevB.61.14095.

(32) Wang, K.; Xu, Y.; Li, Y.; Dravid, V.; Wu, J.; Huang, Y. Sodium Storage in Hard Carbon with Curved Graphene Platelets as the Basic Structural Units. *J. Mater. Chem. A* **2019**, *7* (7), 3327–3335. https://doi.org/10.1039/C8TA11510A.

(33) Zhen, Y.; Chen, Y.; Li, F.; Guo, Z.; Hong, Z.; Titirici, M. M. Ultrafast Synthesis of Hard Carbon Anodes for Sodium-Ion Batteries. *Proc. Natl. Acad. Sci. U. S. A.* **2021**, *118* (42), 1–7. https://doi.org/10.1073/pnas.2111119118.

(34) Chen, C.; Huang, Y.; Zhu, Y.; Zhang, Z.; Guang, Z.; Meng, Z.; Liu, P. Nonignorable Influence of Oxygen in Hard Carbon for Sodium Ion Storage. *ACS Sustain. Chem. Eng.* **2020**, *8* (3), 1497–1506. https://doi.org/10.1021/acssuschemeng.9b05948.

(35) Sing, K. S. W. Reporting Physisorption Data for Gas / Solid Systems with Special Reference to the Determination of Surface Area and Porosity. *Pure Appl. Chem.* **1985**, *57* (4), 603–619. https://doi.org/10.1351/pac198557040603.

(36) Morikawa, Y.; Nishimura, S. ichi; Hashimoto, R. ichi; Ohnuma, M.; Yamada, A. Mechanism of Sodium Storage in Hard Carbon: An X-Ray Scattering Analysis. *Adv. Energy Mater.* **2020**, *10*, 1903176. https://doi.org/10.1002/aenm.201903176.

(37) Li, Z. H. A Program for SAXS Data Processing and Analysis. *Chinese Phys. C* **2013**, *37* (10). https://doi.org/10.1088/1674-1137/37/10/108002.

(38) Li, A.; Tong, Y.; Cao, B.; Song, H.; Li, Z.; Chen, X.; Zhou, J.; Chen, G.; Luo, H. MOF-Derived Multifractal Porous Carbon with Ultrahigh Lithium-Ion Storage Performance. *Sci. Rep.* **2017**, *7*, 1–8. https://doi.org/10.1038/srep40574.

(39) Jian, Z.; Xing, Z.; Bommier, C.; Li, Z.; Ji, X. Hard Carbon Microspheres: Potassium-Ion Anode Versus Sodium-Ion Anode. *Adv. Energy Mater.* **2016**, *6* (3), 201501874. https://doi.org/10.1002/aenm.201501874.

(40) Li, Y.; Wu, F.; Li, Y.; Liu, M.; Feng, X.; Bai, Y.; Wu, C. Ether-Based Electrolytes for Sodium Ion Batteries. *Chem. Soc. Rev.* **2022**, *51* (11), 4484–4536. https://doi.org/10.1039/d1cs00948f.

(41) Zhu, Y. E.; Yang, L.; Zhou, X.; Li, F.; Wei, J.; Zhou, Z. Boosting the Rate Capability of Hard Carbon with an Ether-Based Electrolyte for Sodium Ion Batteries. *J. Mater. Chem. A* **2017**, *5* (20), 9528–9532. https://doi.org/10.1039/c7ta02515g.

(42) Stratford, J. M.; Allan, P. K.; Pecher, O.; Chater, P. A.; Grey, C. P. Mechanistic Insights into Sodium Storage in Hard Carbon Anodes Using Local Structure Probes. *Chem. Commun.* **2016**, *52* (84), 12430–12433. https://doi.org/10.1039/c6cc06990h.

(43) Wen, Y.; He, K.; Zhu, Y.; Han, F.; Xu, Y.; Matsuda, I.; Ishii, Y.; Cumings, J.; Wang, C. Expanded Graphite as Superior Anode for Sodium-Ion Batteries. *Nat. Commun.* **2014**, *5* (May), 1–10. https://doi.org/10.1038/ncomms5033.

(44) He, H.; Huang, C.; Luo, C. W.; Liu, J. J.; Chao, Z. S. Dynamic Study of Li Intercalation into Graphite by in Situ High Energy Synchrotron XRD. *Electrochimica Acta*. **2013**, pp 148–152. https://doi.org/10.1016/j.electacta.2012.12.135.

(45) Li, L.; Zhao, S.; Hu, Z.; Chou, S. L.; Chen, J. Developing Better Ester- And Ether-Based Electrolytes for Potassium-Ion Batteries. *Chem. Sci.* **2021**, *12* (7), 2345–2356. https://doi.org/10.1039/d0sc06537d.

(46) Geoffroy, I.; Willmann, P.; Mesfar, K.; Carré, B.; Lemordant, D. Electrolytic Characteristics of Ethylene Carbonate-Diglyme-Based Electrolytes for Lithium Batteries. *Electrochimica Acta*. **2000**, pp 2019–2027. https://doi.org/10.1016/S0013-4686(99)00431-4.

(47) Mogensen, R.; Colbin, S.; Younesi, R. An Attempt to Formulate Non-Carbonate Electrolytes for Sodium-Ion Batteries. *Batteries and Supercaps*. **2021**, pp 791–814. https://doi.org/10.1002/batt.202000252.

(48) Lin, Z.; Xia, Q.; Wang, W.; Li, W.; Chou, S. Recent Research Progresses in Ether- and Ester-Based Electrolytes for Sodium-Ion Batteries. *InfoMat*. **2019**, pp 376–389. https://doi.org/10.1002/inf2.12023.

(49) Lv, Z.; Li, T.; Hou, X.; Wang, C.; Zhang, H.; Yan, J.; Zheng, Q.; Li, X. Solvation Structure and Solid Electrolyte Interface Engineering for Excellent Na+ Storage Performances of Hard Carbon with the Ether-Based Electrolytes. *Chemical Engineering Journal*. **2022**, *430*, 133143. https://doi.org/10.1016/j.cej.2021.133143.

(50) Yi, X.; Li, X.; Zhong, J.; Wang, S.; Wang, Z.; Guo, H.; Wang, J.; Yan, G. Unraveling the Mechanism of Different Kinetics Performance between Ether and Carbonate Ester Electrolytes in Hard Carbon Electrode. *Adv. Funct. Mater.* **2022**, *32* (48), 202209523. https://doi.org/10.1002/adfm.202209523.

(51) Wang, D. W.; Wu, K. H.; Gentle, I. R.; Lu, G. Q. Anodic Chlorine/Nitrogen Co-Doping of Reduced Graphene Oxide Films at Room Temperature. *Carbon N. Y.* **2012**, *50* (9), 3333–3341. https://doi.org/10.1016/j.carbon.2011.12.054.

(52) Araujo, J. R.; Archanjo, B. S.; de Souza, K. R.; Kwapinski, W.; Falcão, N. P. S.; Novotny, E. H.; Achete, C. A. Selective Extraction of Humic Acids from an Anthropogenic Amazonian Dark Earth and from a Chemically Oxidized Charcoal. *Biol. Fertil. Soils* **2014**, *50* (8), 1223–1232. https://doi.org/10.1007/s00374-014-0940-9.

(53) Nagmani.; Puravankara, S.; Verma, P. Jute-Fiber Precursor-Derived Low-Cost Sustainable Hard Carbon with Varying Micro/Mesoporosity and Distinct Storage Mechanisms for Sodium-Ion and Potassium-Ion Batteries. *Langmuir* **2022**, *38* (50), 15703–15713. https://doi.org/10.1021/acs.langmuir.2c02575.

(54) Zhen, Y.; Sa, R.; Zhou, K.; Ding, L.; Chen, Y.; Mathur, S.; Hong, Z. Breaking the Limitation of Sodium-Ion Storage for Nanostructured Carbon Anode by Engineering Desolvation Barrier with Neat Electrolytes. *Nano Energy*. **2020**, *74*, 104895. https://doi.org/10.1016/j.nanoen.2020.104895.

TOC

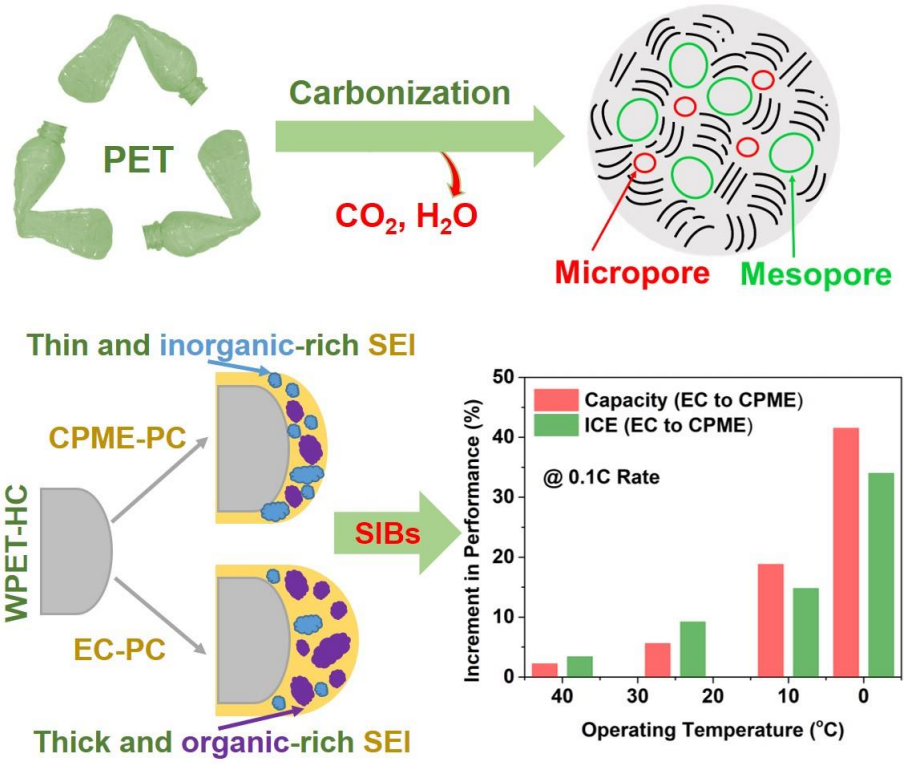
PET
Carbonization
CO_2, H_2O
Micropore
Mesopore
Thin and inorganic-rich SEI
CPME-PC
WPET-HC
EC-PC
Thick and organic-rich SEI
SIBs
Capacity (EC to CPME)
ICE (EC to CPME)
@ 0.1C Rate
Increment in Performance (%)
Operating Temperature (°C)
50
40
30
20
10
0
40
30
20
10
0